Available online at www.sciencedirect.com
SCIENCE DIRECT®
Catalysis Today 100 (2005) 201–215
CATALYSIS TODAY
www.elsevier.com/locate/cattod

# High technology catalysts towards 100% selectivity☆ Fabrication, characterization and reaction studies

G.A. Somorjai*, R.M. Rioux

*Department of Chemistry and Lawrence Berkeley National Laboratory, Materials and Chemical Sciences Division, University of California, Berkeley, CA 94720, USA*

Available online 21 January 2005

**Abstract**

Catalysis in the 20th century focused primarily on activity, increasing turnover rates to produce more molecules per unit time. High selectivity was of lesser concern because disposal of undesirable byproducts was not costly and raw materials were abundant. This has changed in the 21st century because waste disposal is now expensive and the negative ecological impacts are well-documented. As a result, the present focus and roadmap of catalysis science is to achieve high selectivity in all catalyst-based chemical processes. Our knowledge of the molecular ingredients that influence selectivity is poor compared to our understanding of activity. There are six identifiable features that influence both catalyst activity and selectivity. They are metal surface structure, bonding modifier additives, mobility of metal clusters to restructure as well as the mobility of adsorbates on these clusters, selective site blocking, bifunctionality, and oxide-metal interface sites. Identification of the molecular ingredients of catalyst activity and selectivity provides opportunity for catalyst design, combined catalyst synthesis, characterization and reaction studies. In order to obtain high selectivity towards the ultimate goal of 100% selectivity, synthetic methods that enable molecular control over the size, location, structure of the metallic nanoparticles and catalyst promoters must be developed. We are attempting to do this by fabricating two- and three-dimensional catalysts. Two-dimensional nanoparticle or nanowire array catalysts are fabricated by electron beam lithography (EBL) or size reduction lithography (SRL). Arrays with metal surface areas of about 1 $mm^2$ or $10^9$ nanoparticles are fabricated by EBL. These model catalyst systems enable the study of high-turnover reactions such as ethylene hydrogenation. SRL and a lithographic polymer imprinting technique are used to produce nanowire or nanodot array model catalysts with metallic surface areas up to 1 $cm^2$ or $10^{11}$ nanoparticles. High surface area (1 $m^2$ or $10^{15}$ nanoparticles) is produced by a one-step method in which polymer-stabilized monodisperse nanoparticles are synthesized in solution and incorporated into high-surface area mesoporous silica mechanically or through hydrothermal synthesis. Both types of model catalysts are characterized by a variety of physical and chemical techniques and are catalytically active for hydrocarbon conversion test reactions. Our catalyst design approach combines synthesis (fabrication), characterization and reaction studies.


*Keywords:* Catalysis; Selectivity; Activity; Nanoparticles; High technology; Fabrication; Characterization; Reaction studies

## 1. Catalysis in the 20th century

The motivation of catalysis in the 20th century was production (i.e. high activity). As the demand for commodity chemicals boomed, the chemical industry was more concerned with catalyst activity than selectivity [1]. Disposal of unwanted products was inexpensive and the environmental impact of chemical waste disposal was unknown. Fundamental research in heterogeneous catalysis flourished in the 20th century with the introduction of ultrahigh vacuum (UHV) surface science methods and model systems, such as single crystals. These tools and techniques led to an increased molecular understanding of the science of heterogeneous catalysis.

### *1.1. Model catalyst systems and in situ characterization techniques*

The first model system in heterogeneous catalysis was flat, thin films of catalytically relevant metals. Fig. 1

☆ Paper presented at 11th Nordic Symposium on Catalysis in Oulu, Finland, May 23–25, 2004.

* Corresponding author.
*E-mail address:* somorjai@socrates.berkeley.edu (G.A. Somorjai).

0920-5861/$ – see front matter © 2004 Elsevier B.V. All rights reserved.
doi:10.1016/j.cattod.2004.07.059

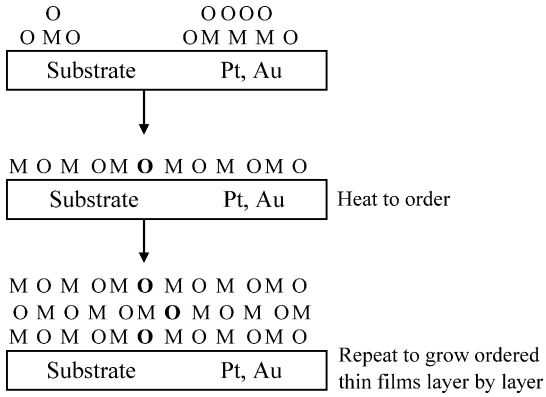


Fig. 1. Preparation of transition metal thin films for adsorption and reaction studies.

Table 1
In situ techniques for studying catalytic reactions under reaction conditions

| |
|---|
| Isotope tracing/exchange techniques |
| Fourier transform infrared spectroscopy (FTIR) |
| Polarization-modulation reflection absorption infrared spectroscopy (PM-RAIRS) |
| Raman spectroscopy (visible, UV, surface enhanced) |
| Infrared-visible sum frequency generation (IV-SFG) |
| Second harmonic generation (SHG) |
| Positron emission ($^{11}$C, $^{13}$N, $^{15}$O) |
| Scanning probe microscopy/spectroscopy (STM/AFM/STS) |
| X-ray absorption spectroscopy (EXAFS, NEXAFS, XANES) |
| Mössbauer spectroscopy |
| Nuclear magnetic resonance (NMR) |
| In situ electron microscopy (controlled atmosphere electron microscopy (CAEM)) |
| High pressure X-ray photoelectron spectroscopy (HP-XPS) |

demonstrates the process by which these films were made. Metal was evaporated onto a substrate and oxidized, upon which it was annealed to order and this process was repeated until the metal film was thick enough to minimize substrate influence. This method of preparation is used to produce films of various metals. These systems provided a wealth of information on the periodic trend of catalytic activity for hydrogenation, dehydrogenation, and H/D exchange reactions [2]. These surfaces were often irreproducible and contained varying concentrations of surface defects.

Single crystals of transition metals were utilized as model systems in heterogeneous catalysis because the surface structure was well defined and easily changed to study its effect on adsorption, reaction and desorption phenomena [3]. The atomic arrangements of four different single crystal surfaces are shown in Fig. 2. The techniques and practices of UHV enabled surface cleaning and characterization in order to obtain a wealth of information on the influence of surface structure on heterogeneous reaction kinetics and dynamics. Stepped and kinked surfaces (such as (7 5 5) and (10 8 7) Miller indices, respectively) are much more active for bond breaking, whereas the closed packed (1 1 1) and (1 0 0) surfaces are less active [4]. These studies demonstrated that defect sites were intimately involved in the observed catalytic chemistry.

A majority of the characterization techniques utilized in the beginning of combined UHV single-crystal research were electron based, therefore, requiring vacuum in order to operate within the constraints of an electron's mean free path. Characterization of the single crystal after high-pressure chemistry was done ex situ, where the sample was removed without exposure to the ambient from high pressure to vacuum. It was suspected and now well-documented that the surface structure under high-pressure reaction conditions is considerably different than a surface in vacuum. In order to bridge the ''pressure gap'' [5] in surface characterization, a number of techniques were adapted or developed to probe the catalyst surface under reaction conditions. Table 1 is a

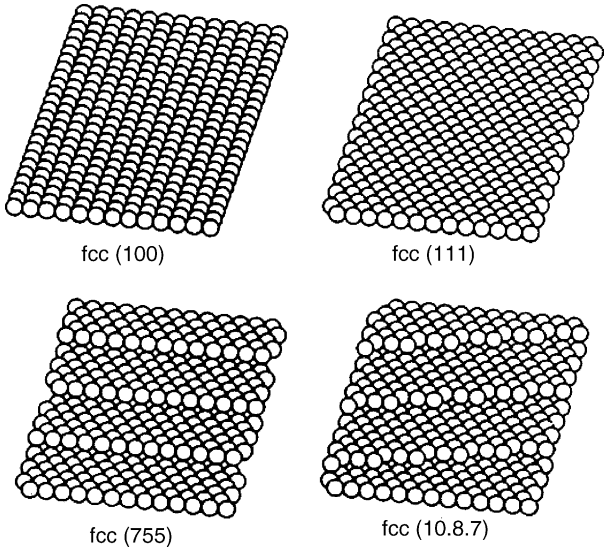


Fig. 2. Single crystal surfaces used for model studies of surface adsorption, reaction and desorption processes.

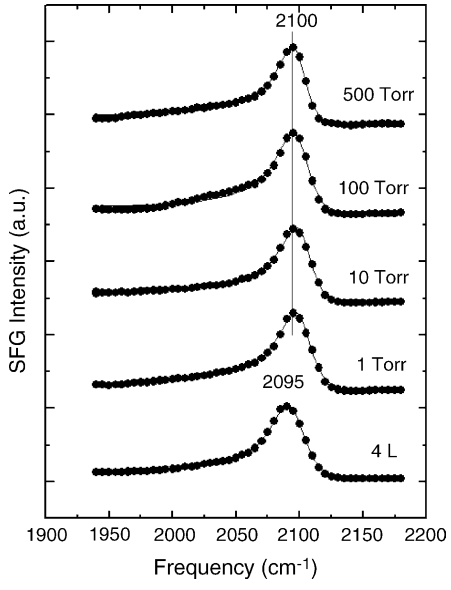


Fig. 3. SFG vibrational spectrum of adsorbed CO in equilibrium with gas phase CO varying over ten orders of magnitude in pressure on Pt(1 1 1) [10].

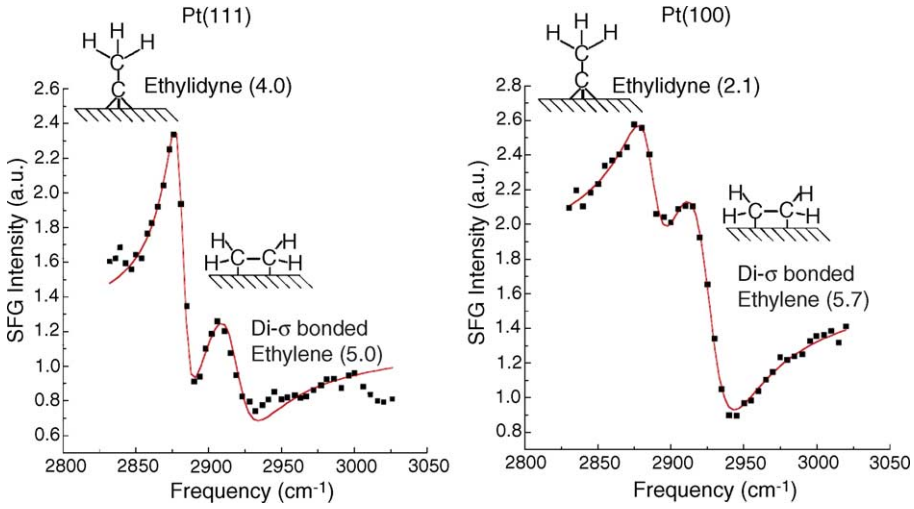


Fig. 4. Detection of reactive intermediates and spectator species during ethylene hydrogenation on Pt(1 1 1) and Pt(1 0 0) at high pressures with SFG surface vibrational spectroscopy [12].

partial list of techniques used to investigate metal surfaces under reaction conditions. Some of the techniques are applicable on both single crystals and industrially significant supported metal nanoparticle catalysts, such as isotope tracing/exchange, FTIR, Raman spectroscopy and EXAFS.

One of the most powerful in situ techniques which optically probes the catalytic surface during turnover is infrared-visible sum frequency generation (IV-SFG) surface vibrational spectroscopy. A detailed description of the sum frequency generation technique can be found in the literature [6–8]. Although this technique has been primarily applied to single crystal surfaces, it has been exploited for studying planar nanoparticle catalysts under high-pressure conditions [9]. SFG has been used to probe high-pressure adsorption of various adsorbates on single crystal surfaces in equilibrium with the gas phase. Fig. 3 is an example of CO adsorption on Pt(5 5 7) with gas phase CO pressure varying over 10 orders of magnitude [10]. Beyond potential attenuation of the IR beam, the isotropic gas phase is SFG inactive, having no influence on the obtained spectrum. Sum frequency generation has been used to identify both spectator and reactive intermediates on a surface during turnover at high pressures. The hydrogenation of ethylene at room temperature proceeds over an ethylidyne-covered surface, a spectator species because it turns over orders of magnitude slower than the reactive intermediate, π-bonded ethylene [11]. SFG has been used to identify ethylidyne and another spectator species during hydrogenation, such as di-σ-bonded ethylene (Fig. 4). At higher hydrogen pressures, the half hydrogenated intermediate, ethyl ($C_2H_5$) has also been identified (Fig. 5) [12].

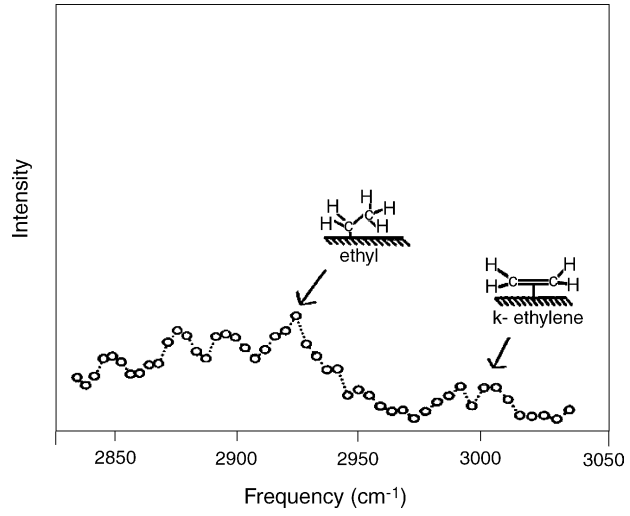


Fig. 5. Detection of half-hydrogenated ethyl ($C_2H_5$) species during ethylene hydrogenation on Pt(1 1 1) at high pressures with SFG surface vibrational spectroscopy [12].

Scanning tunneling microscopy (STM) is the second technique utilized in our laboratory to study catalytic surfaces under reaction conditions. STM does not require a vacuum in order to operate and in principle can be used to study reactions at high pressure or in the liquid phase. A high-pressure–high-temperature STM has been developed in our laboratory, which operates at pressures from $10^{-10}$ to 760 Torr and temperatures as high as 673 K [13]. The structure of adsorbed adlayers in equilibrium with the gas phase has been studied with high-pressure STM. Fig. 6 is an example of high-pressure CO adsorption on Pt(1 1 1) at ambient temperatures. The observed structure ($(\sqrt{19} \times \sqrt{19})R23.4^\circ - 13CO$) of the CO adlayer is different from those observed at low pressures and ambient temperature [14].

## 2. Catalysis in the 21st century

### 2.1. Evolution of the heterogeneous catalyst model system

Single crystals were powerful model systems that provided much of our fundamental understanding of how

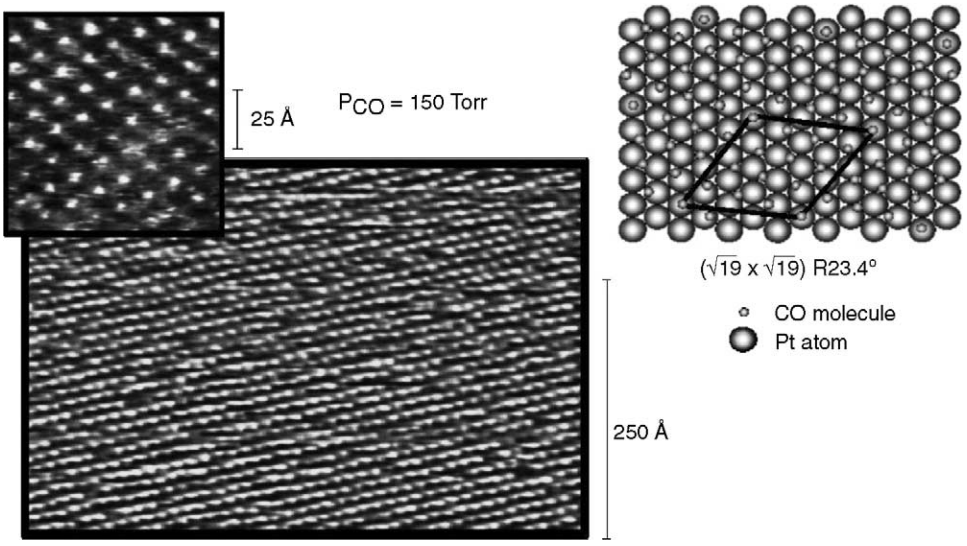


Fig. 6. CO adlayer structure under high-pressure CO on Pt(1 1 1) imaged by high-pressure scanning tunneling microscopy [14].

surface structure dictates activity, and to a lesser extent selectivity. The industrially relevant heterogeneous catalyst is much more complex than a single crystal. Real catalysts are comprised of small metallic crystallites (1–20 nm) dispersed on a high-surface area metal oxide or carbonaceous material [15]. These metallic species can be composed of only a few metal atoms (clusters), while larger metal particles are comprised of 1000s of atoms. Fig. 7 demonstrates for simple cubic atomic packing that the dispersion (ratio of the number of surface atoms to total number of atoms) decreases dramatically as the number of atoms in the cluster (i.e. particle size) increases [16]. The reactivity of atoms in these clusters can be very different from those atoms comprising an extended surface due to interaction with the support material. The support not only stabilizes these small metallic particles, but may also influence the chemistry, through a bifunctional mechanism that provides active sites on the support or at the support-metal interface in addition to the active sites on the metal. Reforming of *n*-hexane to high-octane gasoline on Pt/halogenated $Al_2O_3$ is the most well known example of a bifunctional catalytic mechanism. Hydrogenation/dehydrogenation and dehydrocyclization functions are associated with the metal, while isomerization is associated with acid sites on the $Al_2O_3$ support [17].

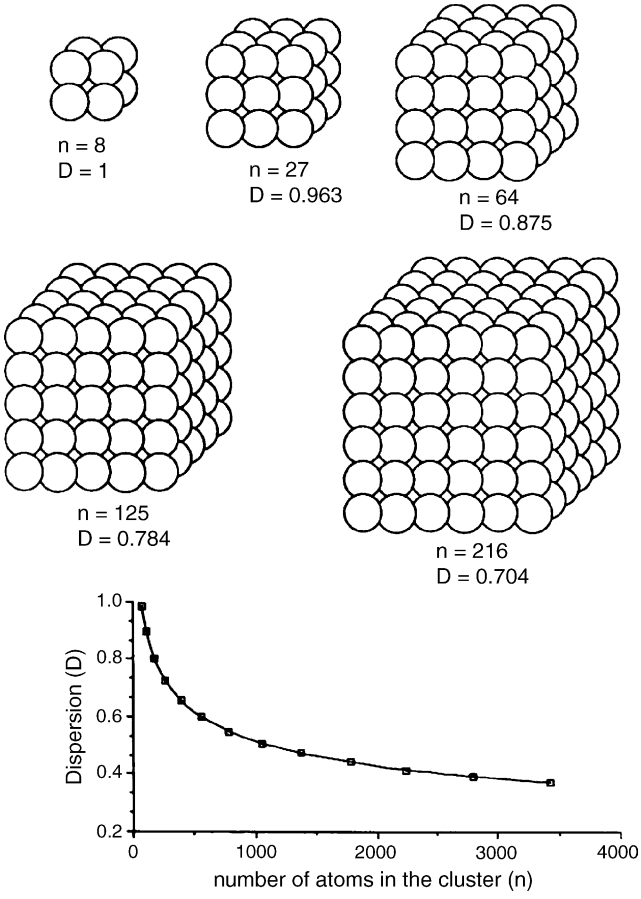


Fig. 7. Dispersion based on a simple cubic packing model for various sized clusters [16].

In an attempt to increase our molecular understanding of the ingredients that influence activity and selectivity, model systems incorporating small metal crystallites and support materials have been designed. Fig. 8 demonstrates the evolution of heterogeneous catalyst model systems in our laboratory with the ultimate goal of producing a replica of an industrial catalyst.

Today in the 21st century, the goal of high selectivity is the driving force for the design of all new catalytic processes. This becomes more difficult as we attempt to develop active and selective catalysts for more difficult catalytic chemistry. For example, the utilization of methane for the production of olefins, and oxygenates currently suffer from poor selectivity at relevant conversion levels [18]. The future of synthetic fuel production from syngas mixtures

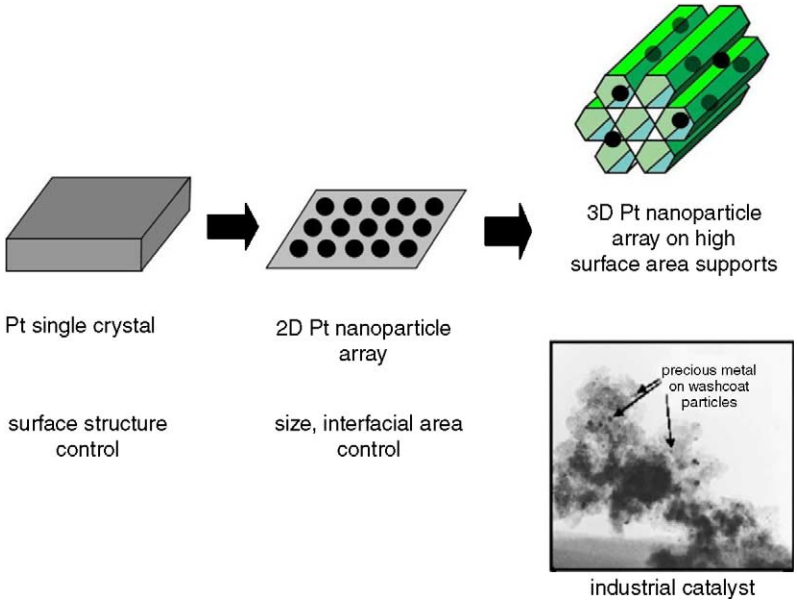


Fig. 8. Evolution of the model system in heterogeneous catalysis.

requires more selective Fischer–Tropsch processes to be developed. Ultimately, a catalyst must possess three characteristics: activity, selectivity and stability and catalyst design of the 21st century must address these three catalyst characteristics. The least understood component is selectivity.

Selectivity represents a new challenge in surface science and catalytic chemistry because the chemical kinetics of selectivity is involved with controlling the activation barriers for numerous elementary reaction steps, whereas with activity, catalysts were designed to minimize the absolute activation barrier of the rate-determining step. Fig. 9 demonstrates this concept on a one-dimensional potential energy surface for a simple parallel reaction. The selectivity to either product at any temperature is determined by the relative difference in barrier height of the two rate-determining steps [19]. From Fig. 9, the larger the relative difference in barrier height, selectivity can be tuned by changing the temperature. Beyond temperature, the kinetics of individual elementary steps may be influenced by properties intrinsic to the catalyst itself. There are six identifiable features of a catalyst that influence activity and selectivity [20]. Examples of four of the six features are summarized in this manuscript. The influence of metal surface structure, selective site blocking, bifunctional catalysis, and metal-oxide interfaces on reaction selectivity will be given.

The isomerization of a light alkane, isobutane as well as its hydrogenolysis is shown in Fig. 10. The metal surface structure plays a decisive role in determining whether isomerization or hydrogenolysis dominates the surface chemistry. The surfaces (shown in Fig. 2) have varying degrees of selectivity for the isomer, *n*-butane [21]. Isomerization is favored over the cubic arranged Pt surface, while increase in kink site density favors selectivity to hydrogenolysis. Kinetic measurements have shown that selectivity during cyclohexene hydrogenation/dehydrogenation reactions is influenced by surface structure [22]. Fig. 11a and b demonstrate at ~400 K, the hydrogenation rate is significantly lower on the (1 0 0) surface relative to the (1 1 1), while the dehydrogenation rate is unaffected by surface structure at 400 K. The selectivity to the dehydrogenated product, benzene is greater on the (1 0 0) surface than on the (1 1 1) surface at temperatures >450 K. Previous work has shown that highly coordinated surface atoms (such as those found on the (1 1 1) surface) are highly selective for hydrogenation [22].

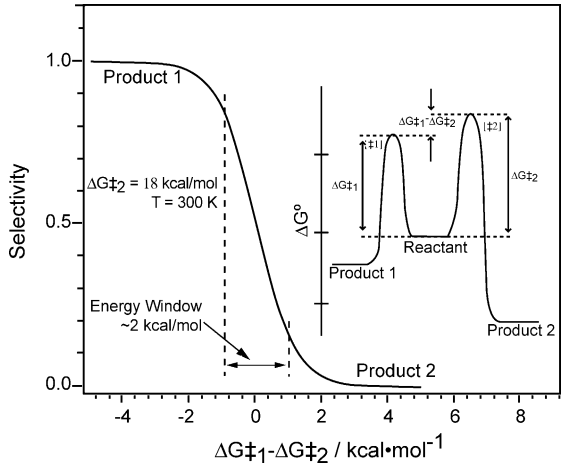


Fig. 9. Effect of relative activation barrier height on reaction selectivity. *Inset:* a one-dimensional potential surface for a parallel reaction. Reaction rates are determined by the absolute barrier heights, $\Delta G_1^{\ddagger}$ and $\Delta G_2^{\ddagger}$, respectively, while selectivity is determined by the difference in barrier heights, $\Delta G_1^{\ddagger} - \Delta G_2^{\ddagger}$ [19].

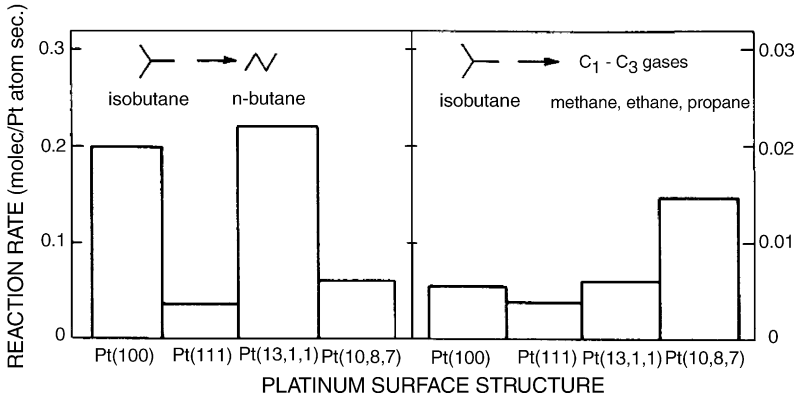


Fig. 10. Influence of Pt surface structure on product distribution (selectivity) for isobutane isomerization and hydrogenolysis. Isomerization is favored over Pt surfaces with a square atomic arrangement, while hydrogenolysis selectivity is maximized when kink site density is high [21].

At higher temperatures where dehydrogenation dominates on both surfaces, SFG has identified two possible reaction intermediates, 1,3 and 1,4 cyclohexadiene (Fig. 12). Both species are reactive intermediates of two distinct dehydrogenation pathways, a fast path proceeding through the 1,3 cyclohexadiene and a slower pathway through the 1,4 intermediate. The observation that 1,3 cyclohexadiene is found on both surfaces suggests that this intermediate is involved in the "fast" pathway, and the 1,4 intermediate turnovers via the "slow" pathway. Sites of lower coordination are more active for dehydrogenation and stepped surfaces are more selective than kinked surfaces, which are also active for hydrogenolysis [23,24].

Selective active site blocking is one of the most effective ways of altering overall reaction selectivity. In some cases, catalysts alter selectivity by poisoning the most active surface sites with carbonaceous deposits [25]. One of the most popular methods to enhance the stability of a reforming catalyst is the addition of second metal. In fact, this method can have a significant impact on selectivity to the products of *n*-hexane reforming. The addition of variable amounts of gold to a Pt(1 1 1) single crystal followed by thermal treatment leads to Au–Pt surface alloys with varying concentration of surface Pt [26]. At low Au addition, the activity to isomerization products, 2- and 3-methylpentane increases until it levels off at intermediate Au additions. Cyclization of *n*-hexane decreases at all levels of Au addition, while dehydrocyclization activity monotonically decreases with increasing Au content. The varying degree of influence of gold addition to a Pt(1 1 1) single crystal leads to substantial changes in selectivity (Fig. 13). Substitution of Pt with gold leads to a dilution of surface Pt and effectively segregates Pt into smaller ensembles, which with the addition of enough gold, may dilute the Pt to isolated single

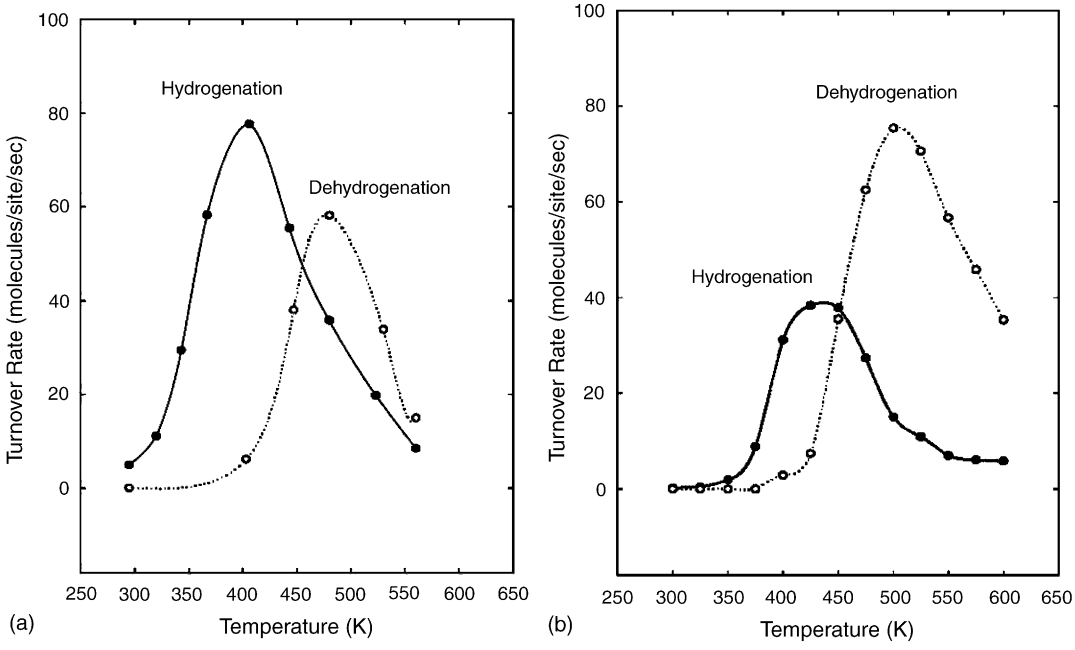


Fig. 11. Kinetic rate data for cyclohexene hydrogenation/dehydrogenation on (a) Pt(1 1 1) and (b) Pt(1 0 0) [22].

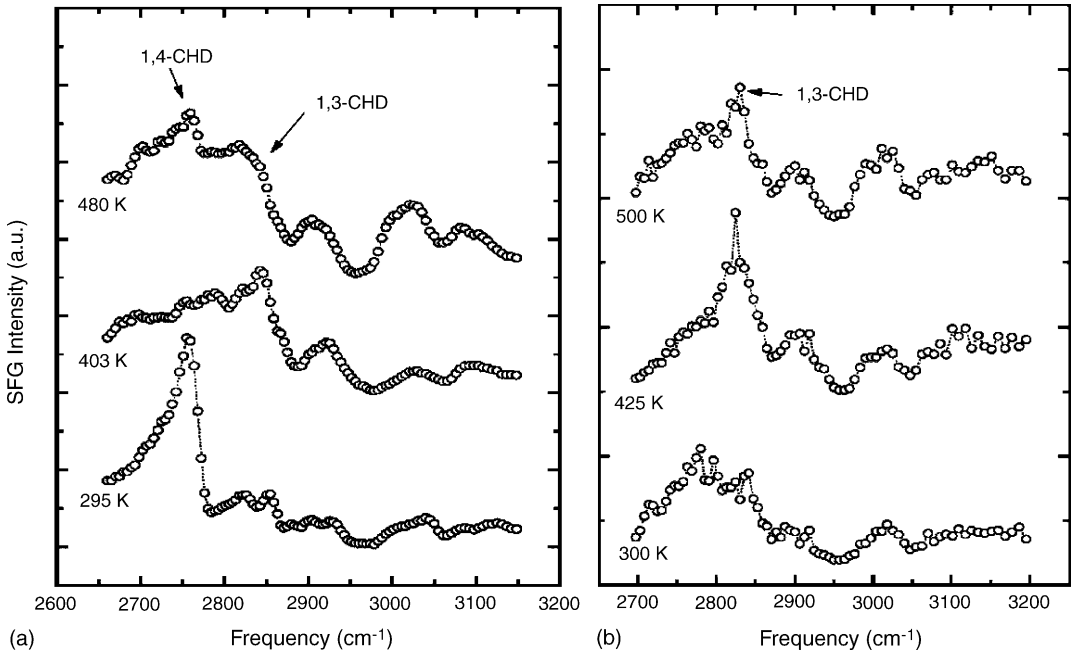


Fig. 12. SFG spectra of cyclohexene hydrogenation/dehydrogenation on (a) Pt(1 1 1) and (b) Pt(1 0 0) [22].

atoms. This method of site blocking is selective because larger ensembles are eliminated much faster than bridge or atop sites and chemistry which turnovers on these larger ensembles (active site) will be affected to a greater extent.

The third component of a supported nanoparticle catalyst that can affect reaction selectivity is the dual function of the metal nanoparticle and support in some catalytic chemistry. The support itself may also be active and promote chemical transformation in sequence or parallel with the chemistry occurring on the metal [27]. They may function in sequence to produce a specific molecule, one that would not be formed without both the metal nanoparticle and support. A schematic representation of bifunctional catalysis relevant to catalytic reforming is shown in Fig. 14. According to a model proposed by Heinemann and co-workers [17], the mechanism for *n*-hexane dehydrocyclization to benzene is the initial dehydrogenation of *n*-hexane to *n*-hexene on a metal site, isomerization of *n*-hexene to methylcyclopentane on an acid site, dehydrogenation to methylcyclopentene on a metal site, isomerization to cyclohexene on an acid site, then dehydrogenation on a metal site to cyclohexadiene, followed by further dehydrogenation to benzene. The mechanism for dehydrocyclization is complex and each possible step requires one of the two functions to proceed.

Supported catalysts possess oxide-metal interfaces that are absent from the extended single crystal surface. The nature of this oxide-metal interface is unknown but significant evidence exists suggesting that it is highly active and capable of altering reaction selectivity. Reducible

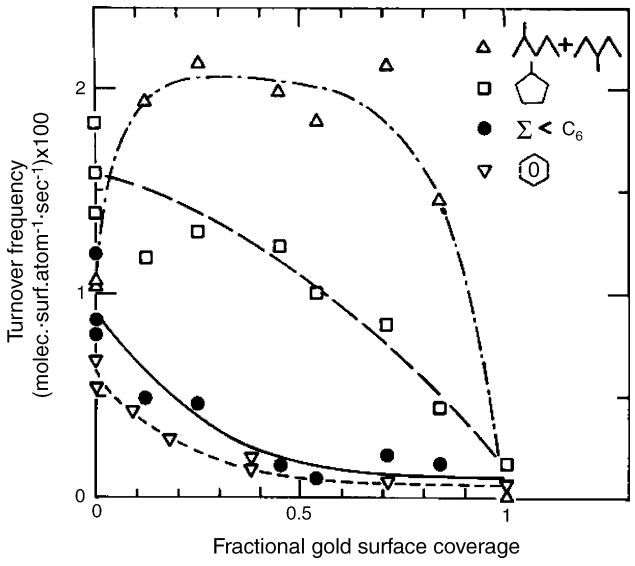


Fig. 13. Initial turnover frequencies for the formation of reforming products from *n*-hexane conversion as a function of fractional gold coverage for Au–Pt(1 1 1) alloys [26].

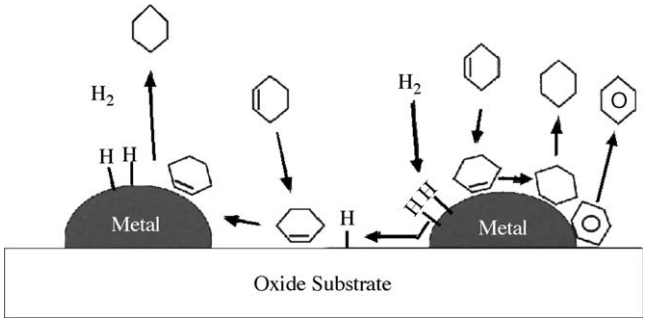


Fig. 14. Schematic representation of bifunctional catalysis.

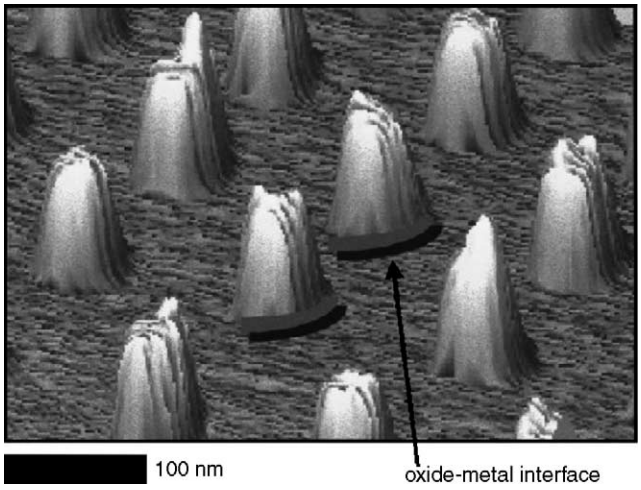


Fig. 15. Oxide-metal interface on a model Pt nanoparticle array catalyst, which maybe responsible for the well-documented strong metal-support interaction (SMSI).

oxides, such as $TiO_2$ are well known for metal-support interactions with small metal crystallites [28,29] possibly providing sites of high Lewis acidity. Fig. 15 is an example of a metal-support interface where these strong interactions may occur on a $Pt/Al_2O_3$ nanoparticle array catalyst.

## 3. Fabrication of high-technology catalysts

The goal of fabricating high-technology catalysts is to develop a catalyst which provides the highest possible selectivity. Our approach is to fabricate two- and three-dimensional nanocatalysts with molecular control of the parameters discussed above. Using lithographic techniques for nanoparticle array fabrication and combined nanoparticle/mesoporous metal oxide synthesis for high-surface area nanocatalysts, we are able to exert control on the size and structure of the metal particle, location within the support matrix, and promoter addition.

### *3.1. Fabrication and characterization of two-dimensional nanoparticle array catalysts*

The first nanoparticle arrays were constructed using electron beam lithography (EBL) [30,31], a technology utilized for high-resolution pattern writing using a highly collimated electron beam and an electron sensitive resist. Nanoparticle arrays are built in a top down approach on a Si(1 0 0) wafer which is covered with a 15 nm thick layer of $SiO_2$ or $Al_2O_3$ followed by thermal treatment in air at 1073 K. After annealing, a layer of polymethylmethacrylate (PMMA) is spin-coated onto the oxide. After irradiation by an electron beam to create the array pattern, PMMA damaged by electron beam exposure is removed in developer solution. After PMMA removal, a 15 nm Pt film is deposited on the surface by electron beam evaporation, followed by standard liftoff procedures involving acetone rinse and ultrasonication to remove the remaining polymer. Fig. 16 is a schematic of the EBL process. After metal deposition, a total Pt surface area of $\sim$1 $mm^2$ is obtained. An electron microscopy image and diffraction pattern of the Pt nanoparticle arrays are shown in Fig. 17. Electron diffraction of the nanoparticle arrays reveal the polycrystalline nature of the Pt nanoparticles. Upon thermal treatment in vacuum, hydrogen or oxygen, Pt particles became single crystalline [32,33]. The arrays require cleaning before they can be used in catalytic reactions. Ion sputtering is generally a sufficient technique for cleaning single crystal surfaces, but sputtering was determined to be destructive to the Pt nanoparticle array model catalysts. Bombardment of the Pt array with 1 kV $Ne^+$ ions causes the particles to be buried into the $SiO_2$ or $Al_2O_3$

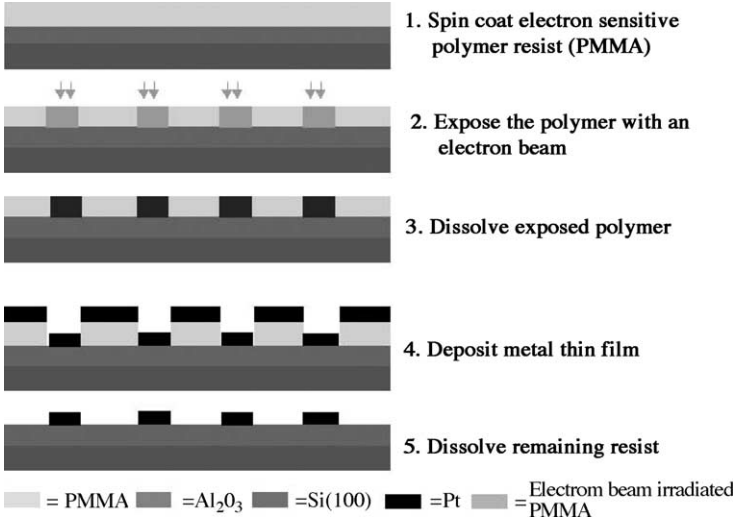


Fig. 16. Schematic representation of the electron beam lithography (EBL) process used to fabricate two-dimensional Pt nanoparticle array catalysts [35].

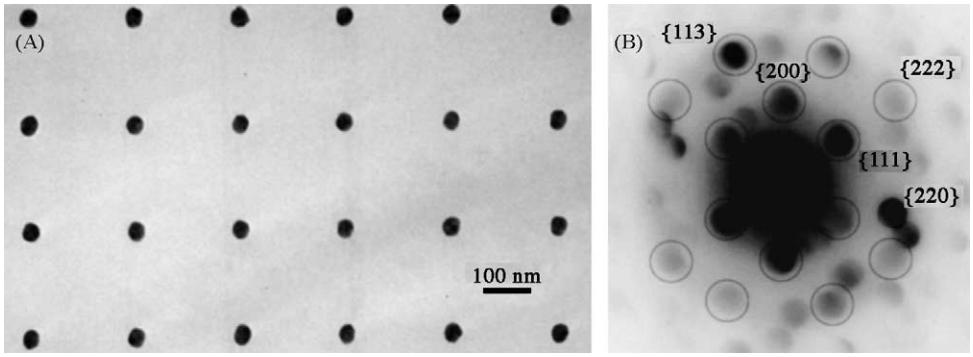


Fig. 17. Characterization of Pt nanoparticle array catalysts. (A) Electron microscopy image of the as-fabricated Pt nanoparticle array and (B) electron diffraction pattern demonstrating polycrystalline nature of the as-fabricated arrays [32].

layer [33,34]. Combined high-temperature oxidation (calcination) and reduction cycles were insufficient for cleaning the nanoparticle arrays. Rather, using low pressures ($1 \times 10^{-6}$ Torr) of $NO_2$ at 573 K, the major contaminant, carbon is removed from the catalyst surface. Adsorbed oxygen from $NO_2$ decomposition is titrated with 10 L CO (1 L = $10^{-6}$ Torr s) after which the wafer is flashed to 573 K to remove adsorbed CO and $CO_2$. Auger electron spectroscopy demonstrates that this method safely and effectively cleans the nanoparticle arrays. Ethylene hydrogenation, a structure insensitive reaction has been chosen as a probe reaction for these clean Pt nanoparticle arrays [35]. Measured kinetic parameters, apparent activation energy and reaction order in ethylene and $H_2$ are in agreement with previous results reported on a Pt(1 1 1) single crystal [36] at similar conditions. The kinetic behavior of the single crystal and nanoparticle array confirm that the Pt nanoparticles are clean and comparable to the extended Pt surface. Upon addition of CO which poisons the ethylene hydrogenation reaction, the behavior of the Pt(1 1 1) and Pt nanoparticles on $Al_2O_3$ differs markedly from each other (Fig. 18). Addition of 1 Torr CO led to a doubling of the apparent activation energy to 20 kcal mol$^{-1}$ on Pt(1 1 1), while addition of a similar amount of CO led to a minimal increase in the activation energy on the Pt nanoparticle array. The doubling of the apparent activation energy in the case of the Pt single crystal is due to CO site blocking, requiring CO desorption to open a minimum number of sites to adsorb ethylene. Sum frequency investigations of ethylene and CO co-adsorption demonstrated that high-pressure ethylene (35 Torr) was unable to displace preadsorbed CO, but preadsorbed π-bonded ethylene was easily displaced by high-pressure CO (>0.1 Torr) leaving CO co-adsorbed with ethylidyne [37]. Higher pressures of CO (>1 Torr) were required to displace ethylidyne from the surface. Additional kinetic data demonstrated that the addition of CO completely poisoned the ethylene hydrogenation reaction at temperatures less than 400 K. In the case of the nanoparticle array, the activation energy is unchanged by CO addition suggesting that there are domains where Pt remains free of CO and ethylene can adsorb and turnover [38]. The Pt sites located at the metal-oxide interface have been implicated as the source of free Pt. Studies of other model hydrocarbon reactions, such as cyclohexene hydrogenation/dehydrogenation [33], have confirmed that the Pt arrays are appropriate catalyst models.

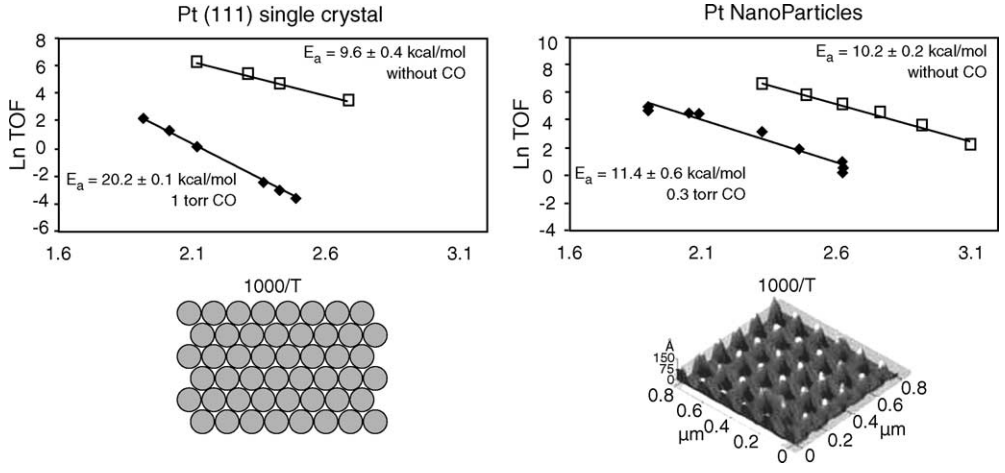


Fig. 18. Arrhenius plot for ethylene hydrogenation in the presence and absence of CO on a Pt(1 1 1) single crystal and Pt nanoparticle array catalyst [38].

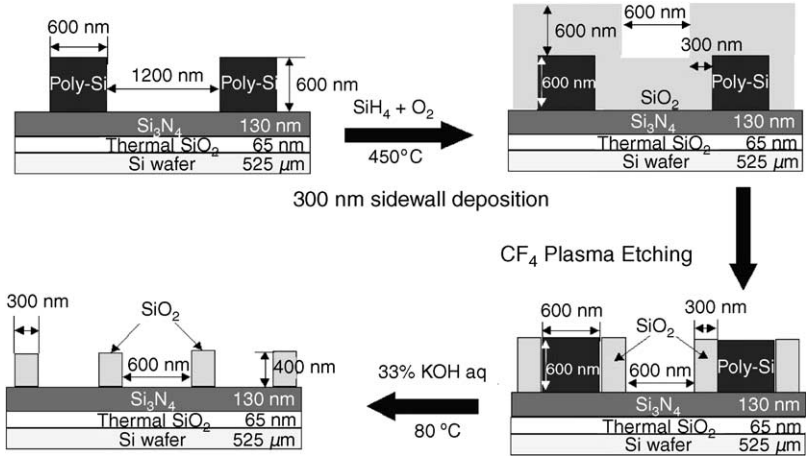


Fig. 19. Overall scheme for size reduction lithography (SRL) [39].

The limitations of EBL (low throughput and high cost) and the necessity for higher metal surface areas (∼1 $cm^2$ or $10^{11}$ nanoparticles) requires the development of a high throughput, low cost technique. A method called size reduction lithography (SRL) [39] developed at Berkeley enables 7 nm features to be fabricated from 600 nm features initially prepared by photolithography (Fig. 19). The method requires several repetitions to reduce the 600 nm features to silicon nanowires of ∼7 nm. An example of the SRL mold after three consecutive cycles is shown in Fig. 20. Once this mold has been fabricated, the pattern is transferred into PMMA under high pressure and elevated temperatures using nanoimprint lithography (NIL). After transferring, residual PMMA is removed to expose the thermal oxide layer by oxygen plasma etching. Finally, Pt is deposited via electron beam evaporation. Fig. 21 is a scanning electron micrograph of the final product, 22 nm wide Pt nanowires. Further details on the fabrication of nanowires by SRL and NIL are found elsewhere [40]. The nanowire catalysts are cleaned by the same method used for the EBL samples and are active for ethylene hydrogenation, although the observed kinetic parameters on the Pt nanowire samples suggests the wire surface is not completely clean [41].

A new method, which has recently been developed for the production of nanoparticle array catalysts, is through the use of a nanostencil [42,43]. This method has the advantage of directly producing high-density nanoparticle arrays. The nanostencil is made from a silicon nitride membrane and its fabrication is outlined in Fig. 22. Starting with a silicon wafer, one side is coated with $Si_3N_4$ and the other side with a photoresist. A portion of the photoresist is removed by reactive ion etching to expose the silicon wafer. A wet etch of KOH is used to remove the exposed silicon wafer to the silicon nitride layer on the other side of the wafer. After this step, photoresist is deposited onto the silicon nitride layer and a pattern is cut into the photoresist by EBL. Using the photoresist as a hard mask, the pattern is transferred into the silicon nitride layer by reactive ion etching. After stripping

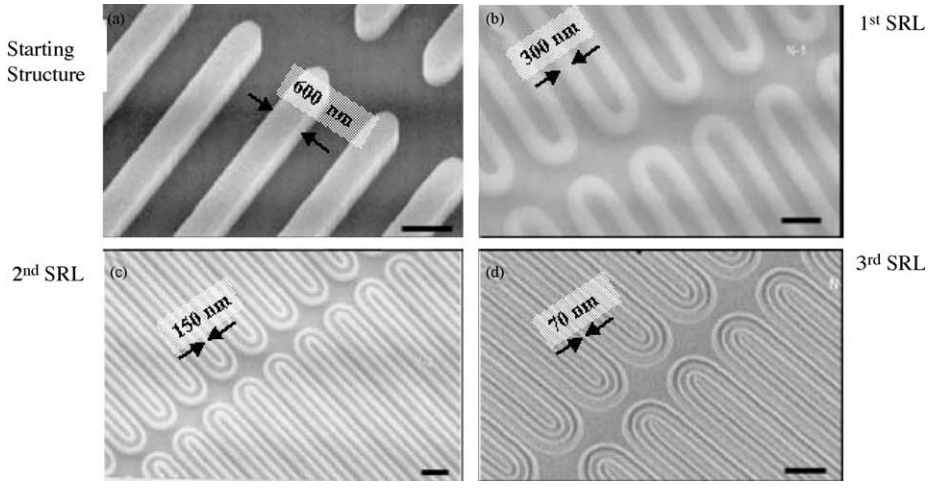


Fig. 20. Multiplication of pattern density by SRL. Field emission scanning electron microscopy (FESEM) images (a) after patterning sacrificial poly-Si layer, (b) after $SiO_2$ deposition, $SiO_2$ spacer etch by $CF_4$ plasma, and removal of sacrificial poly-Si by KOH, (c) after poly-Si deposition, poly-Si spacer etch by $Cl_2$ and HBr, and removal of $SiO_2$ by HF and (d) after $SiO_2$ deposition, $SiO_2$ spacer etch by $CF_4$ plasma, and removal of sacrificial poly-Si by KOH. Eight ($=2^3$) lines were generated after three SRL cycles. Line width was 70 nm and spacing was 80 nm in (d). The scale bars are 1 μm [39].

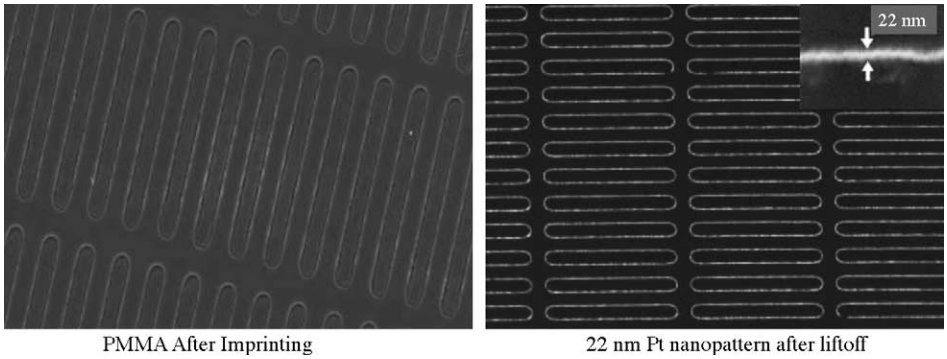


Fig. 21. Pattern transfer by nanoimprint lithography (NIL) into PMMA and final nanowire catalyst after metal deposition and liftoff [40].

the unwanted photoresist, the final product is a $Si_3N_4$ nanostencil.

Pt nanodot arrays are made by depositing platinum through the nanostencil directly onto an oxide-coated Si(1 0 0) wafer. The silicon nitride nanostencil has micron-sized spacings ($a \times a$). In order to increase the number density of the Pt nanodots as well as reduce the spacings between the nanodots, the substrate or the nanostencil is stepped on the nanoscale and Pt is again deposited. After four nanoscale steps and Pt evaporations, the spacing between the nanoparticles is decreased from ($a \times a$) to ($a/2 \times a/2$) and the Pt atom density increases by a factor of 4. Nanostencil patterning is a promising technique for directly producing high-density nanoparticle arrays and future work on these arrays will consist of characterization and reaction studies.

### 3.2. Fabrication and characterization of high-surface area three-dimensional nanoparticle catalysts

Supported transition metal catalysts generally have metallic surface areas of 1 $m^2\,g^{-1}$ or greater. EBL or SRL are unable to produce metallic nanowires or particles of this number density. Metal surface areas of this magnitude can only be obtained in three-dimensional structures. The advantage of both lithographic techniques lies in their systematic control of particle (or wire) size and pitch (interparticle spacing) during fabrication. This ability to rationally tune with a high degree of control is also required for synthesis of a high-surface area model catalyst. This has been achieved with two novel methods of catalyst fabrication (Fig. 23). In both methods, nearly monodispersed Pt nanoparticles are initially fabricated by modified

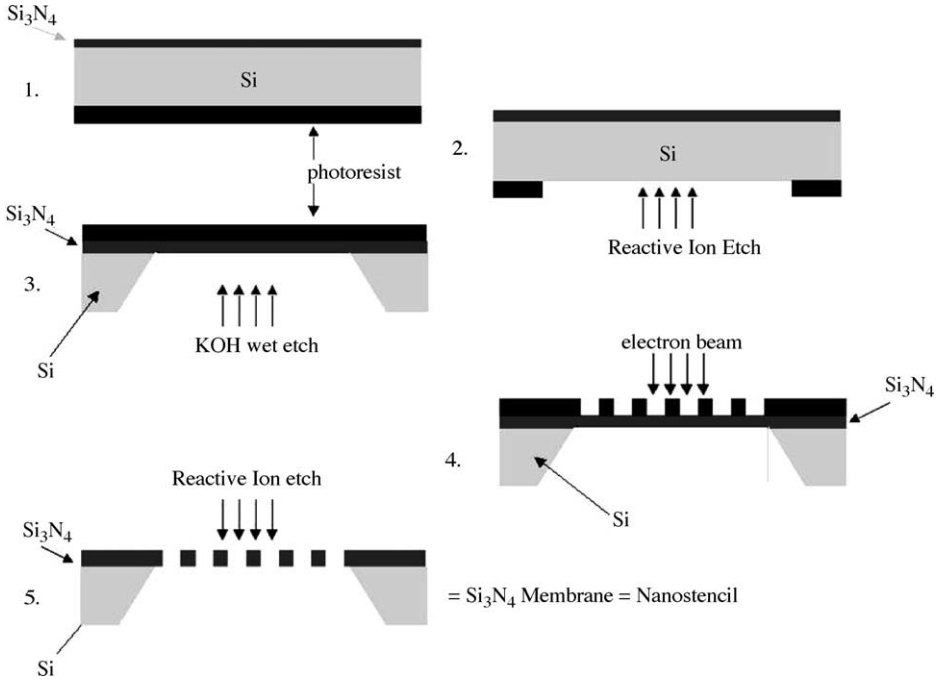


Fig. 22. Fabrication of $Si_3N_4$ nanostencil for production of high-density (1 $cm^2$) nanoparticle array catalysts.

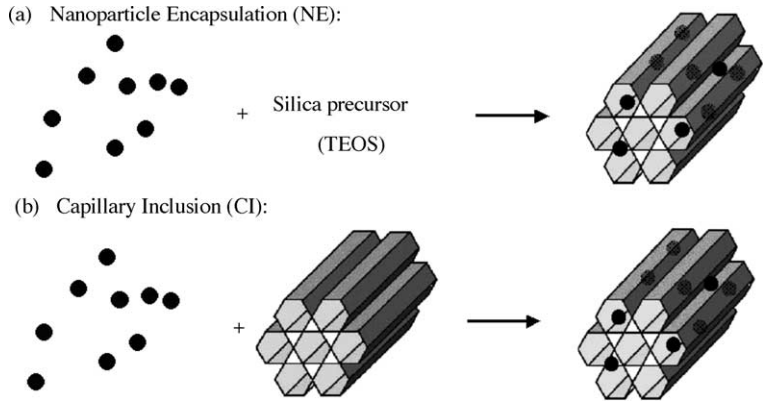


Fig. 23. Synthetic schemes for (a) nanoparticle encapsulation and (b) capillary inclusion.

alcohol reduction (or $H_2$ reduction) methods presented in the literature [44–46]. TEM micrographs of 1.7–7.1 nm Pt nanoparticles are shown in Fig. 24. The first method of catalyst synthesis involves the hydrothermal synthesis of SBA-15 silica in a solution containing polymer stabilized Pt nanoparticles. This method, referred to as nanoparticle encapsulation (NE) leads to Pt/SBA-15 catalysts with particles situated within the silica pore structure. The modified synthesis and characterization of these catalysts can be found elsewhere [47,48].

The second method of synthesis called capillary inclusion (CI) requires independent synthesis of monodisperse Pt nanoparticles and mesoporous SBA-15 silica [49], followed by mixing in water/ethanol solution with low power sonication to promote nanoparticle entry into the SBA-15 pore structure by capillary inclusion and mechanical agitation [50]. Fig. 25 is an example of as-prepared ∼1% Pt/SBA-15 by capillary inclusion with three different Pt particle sizes (1.7, 2.6, 3.6 nm). After synthesis, catalysts are calcined and reduced to remove the stabilizing polymer and adsorbed oxygen. These catalysts have been characterized by a number of physical and chemical techniques, which confirm that Pt has been incorporated into the SBA-15 channels and chemically accessible after removal of the stabilizing polymer. Chemisorption of $H_2$, CO and $H_2$–$O_2$ titration confirm that the calcination/reduction procedure exposes a metallic Pt surface. Pt/SBA-15 catalysts were active for two hydrocarbon test reactions, ethylene hydrogenation and ethane hydrogenolysis [50]. Ethane hydrogenolysis was found to be structure sensitive with smaller particles displaying higher activity, suggesting that coordinatively unsaturated surface atoms prevalent in small Pt clusters are more active for hydrogenolysis. This trend is consistent with theoretical work which suggests that the these low coordination sites provide more stable binding for $C_2H_x$ species and their corresponding activated complexes

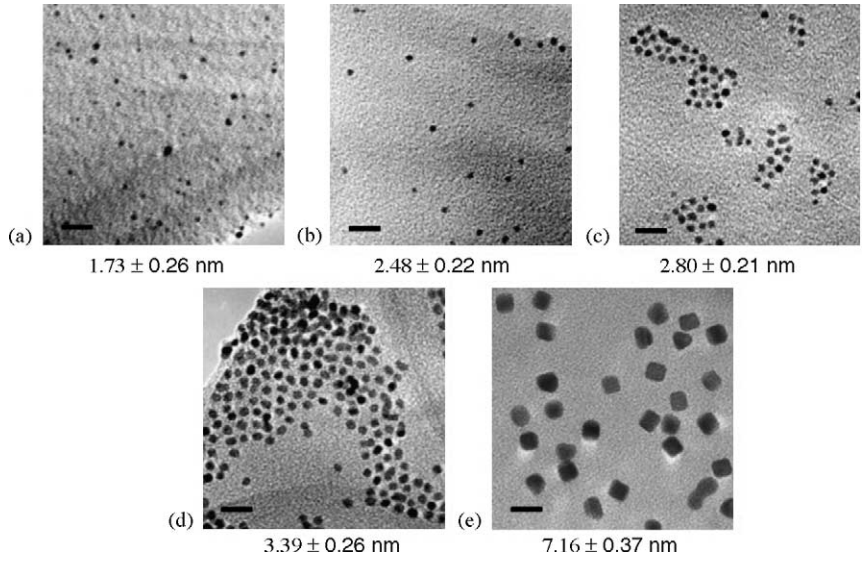


Fig. 24. TEM micrographs of polymer stabilized Pt nanoparticles: (a) 1.7 nm, (b) 2.6 nm, (c) 2.9 nm, (d) 3.6 nm and (e) 7.1 nm [50]. Number average particle sizes determined by counting 200 particles.

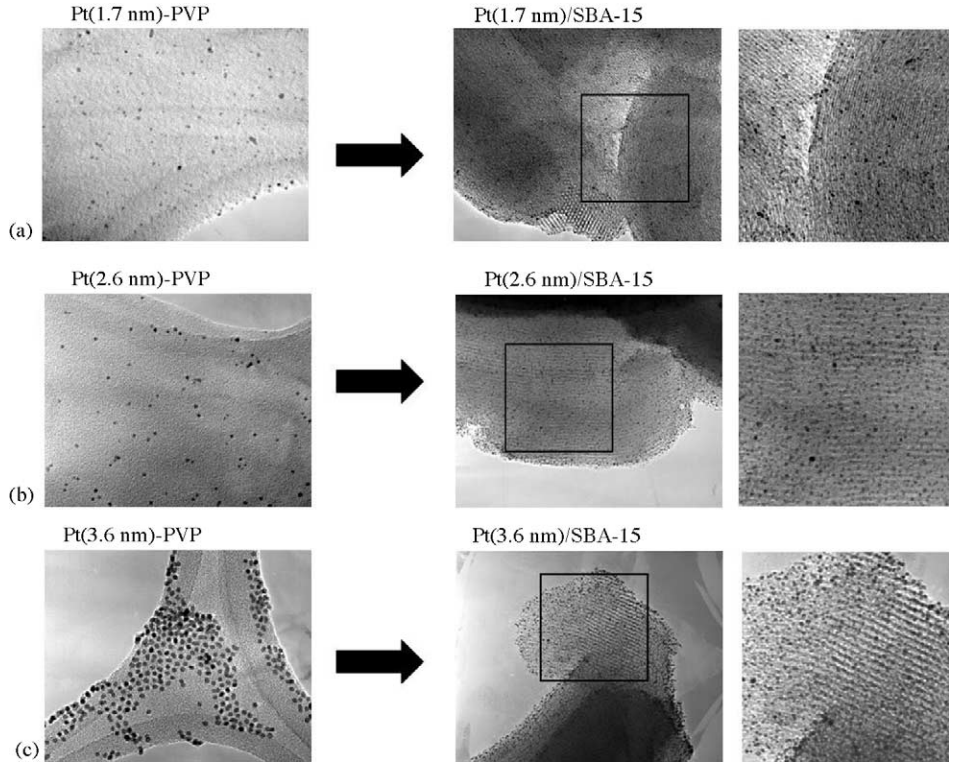


Fig. 25. Pt supported catalysts prepared by capillary inclusion (CI) method: (a) 1.7 nm, (b) 2.6 nm and (c) 3.6 nm [50].

[51,52]. Continuing work on these materials is focusing on the effect of particle size on reaction selectivity. Cyclohexene hydrogenation/dehydrogenation and *n*-hexane reforming are our current focus [53].

### *3.3. Synthesis, characterization and reaction studies of isolated Pt nanoparticle coreshell materials*

The ability to isolate individual nanoparticles has important implications in catalyst activity, selectivity and stability. Isolation of nanoparticles reduces the likelihood of sintering and activity and selectivity can be affected in a shape selective type mechanism if the pore structure of the isolating material is of molecular dimensions. Selectivity may be enhanced through minimization of secondary reactions and if the metal-oxide interface is of importance to the catalytic chemistry, these materials maximize the area of this interface.

We have recently developed hollow coreshell materials of two different cobalt sulfide phases and cobalt oxide [54]. The hollow coreshell materials are formed on the nanoscale by a mechanism called the Kirkendall effect [55]. The effect demonstrates that atomic diffusion occurs through vacancy exchange and not the direct interchange of atoms. In a binary diffusion couple, one of the species diffuses into the other species at a much faster rate, and the net directional flow of matter is balanced by an opposite flow of vacancies. If the faster diffusing species is confined to the nanocrystal core, the net rate of vacancy formation should increase dramatically because of the high surface to volume ratio inherent to nanocrystals [55]. Fig. 26 is an example of $Co_3S_4$ and $Co_9S_8$ hollow nanocrystal formation, respectively.

Coreshell materials of catalytic relevance were synthesized by a three-step process. Platinum particles were synthesized according to literature methods [56], followed by injection and decomposition of $Co_2(CO)_8$ to form Pt/Co coreshell nanoparticles, and the introduction of oxygen to transform the Co into CoO hollow structures. The resulting material is a hollow CoO shell with a Pt nanoparticle in the interior (Fig. 27). X-ray diffraction data confirmed no Co–Pt alloy formation and high-resolution TEM confirmed the CoO shell is multi-crystalline suggesting that gases gain access to the Pt particle via diffusion along grain boundaries. Ethylene hydrogenation was chosen, as a simple test reaction and the Pt/CoO coreshell material were active at temperatures as low as 208 K. Table 2 is comparison of ethylene hydrogenation turnover rates of the coreshell material compared with standard supported and model Pt catalysts. Coreshell catalysts are less active than a standard supported Pt catalyst or single crystal. Coreshell materials have not been subjected to high temperature reduction because CoO is reduced to metallic cobalt at high temperatures in hydrogen, destroying the coreshell structure. The coreshell structure can also be destroyed at higher temperatures in an inert atmosphere. Although ethylene hydrogenation occurs in a net-reducing environment, the

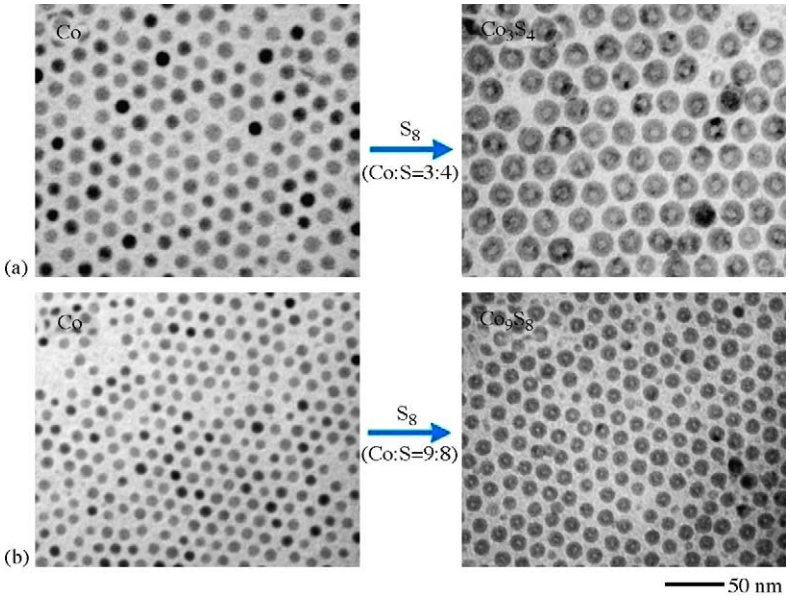


Fig. 26. Formation of (a) $Co_3S_4$ and (b) $Co_9S_8$ hollow nanoparticles by the nanoscale Kirkendall effect [54].

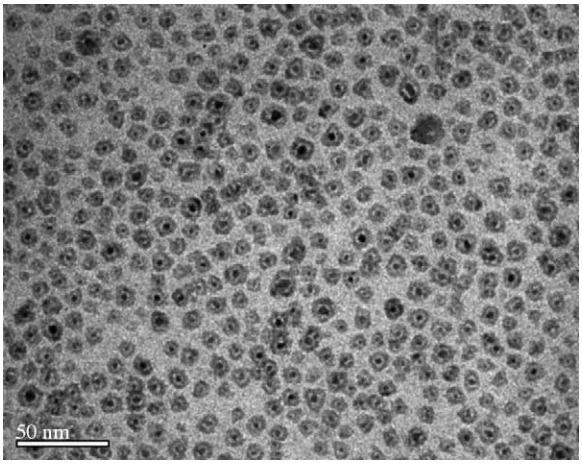


Fig. 27. Electron microscopy image of as-synthesized Pt/CoO coreshell nanocatalyst [54].

lower activity of the coreshell materials is attributed to an incomplete reduction of the Pt surface. Pt coreshell materials of more stable oxides, such as $TiO_2$ and $Al_2O_3$ with a porous coreshell structure are currently being synthesized.

Table 2
Reaction rate data for ethylene hydrogenation on Pt/CoO coreshell materials and selected Pt catalysts

| Catalyst | Turnover frequency ($s^{-1}$)[a] | $E_a$ (kcal $mol^{-1}$) |
|---|---|---|
| Pt nanoparticle arrays[b] | 14.35 | 10.2 |
| Pt single crystal[c] | 9.28 | 10.8 |
| 0.04% Pt/$SiO_2$[d] | 4.36 | 8.6 |
| Pt wire[d] | 2.65 | 8.6 |
| 14.2% Pt (5.4 nm)/CoO coreshell | 0.288 | 5.0 |

[a] Rates corrected to 10 Torr $C_2H_4$, 100 Torr $H_2$ and 298 K.
[b] From ref [35].
[c] From ref [36].
[d] From ref [57].

## Acknowledgements

This work is supported by the Director, Office of Energy Research, Office of Basic Energy Sciences, Materials and Chemical Sciences Divisions of the U.S. Department of Energy under Contract No. DE-AC03-76SF00098. R.M. R. would like to acknowledge the Ford Motor Company and the Berkeley Catalysis Center for financial support.

## References

[1] G.A. Somorjai, K. McCrea, Appl. Catal. A 222 (2001) 3.
[2] R.S. Dowie, D.A. Whan, C. Kemball, J. Chem. Soc. Faraday T. 68 (1972) 2150.
[3] G.A. Somorjai, Science 227 (1985) 902.
[4] S.L. Bernasek, G.A. Somorjai, J. Chem. Phys. 62 (1975) 3149.
[5] G.A. Somorjai, Appl. Surf. Sci. 121 (1997) 1.
[6] Y.R. Shen, Nature 337 (1989) 519.
[7] Y.R. Shen, The Principles of Nonlinear Optics, Wiley, New York, 1984.
[8] G.A. Somorjai, K.R. McCrea, Adv. Catal. 45 (2000) 386.
[9] S. Baldelli, A.S. Eppler, E. Anderson, Y.R. Shen, G.A. Somorjai, J. Chem. Phys. 113 (2000) 5432.
[10] K. R. McCrea, Ph.D. Thesis, University of California, Berkeley, 2001.
[11] S.M. Davis, F. Zaera, B.E. Gordon, G.A. Somorjai, J. Catal. 92 (1985) 240.
[12] P.S. Cremer, X.C. Shen, G.A. Somorjai, J. Am. Chem. Soc. 118 (1996) 2942.
[13] B.J. McIntyre, M. Salmeron, G.A. Somorjai, Catal. Lett. 14 (2000) 263.
[14] D. Tang, K. Hwang, M. Salmeron, G.A. Somorjai, J. Phys. Chem. B 108 (2004) 13300.
[15] J.R. Anderson, Structure of Metallic Catalysts, Academic Press, London, 1975.
[16] R. van Hardeveld, F. Hartog, Surf. Sci. 15 (1969) 189.
[17] G.A. Mills, H. Heinemann, T.H. Milliken, A.G. Oblad, Ind. Eng. Chem. 45 (1953) 134.
[18] J.H. Lunsford, Catal. Today 63 (2000) 165.

[19] F. Zaera, J. Phys. Chem. B 106 (2002) 4043.
[20] J. Grunes, J. Zhu, G.A. Somorjai, Chem. Commun. 18 (2003) 2257.
[21] S.M. Davis, F. Zaera, G.A. Somorjai, J. Am. Chem. Soc. 104 (1982) 7453.
[22] K.R. McCrea, G.A. Somorjai, J. Mol. Catal. A 163 (2000) 43.
[23] G.A. Somorjai, D.W. Blakely, Nature 258 (1975) 580.
[24] D.W. Blakely, G.A. Somorjai, J. Catal. 42 (1976) 181.
[25] F. Zaera, G.A. Somorjai, Langmuir 2 (1986) 686.
[26] J.W.A. Sachtler, G.A. Somorjai, J. Catal. 81 (1983) 77.
[27] M. Boudart, G. Djéja-Mariadassou, Kinetics of Heterogeneous Catalytic Reactions, Princeton University Press, Princeton, 1984.
[28] S.J. Tauster, S.C. Fung, R.L. Garten, J. Am. Chem. Soc. 100 (1978) 170.
[29] S.J. Tauster, S.C. Fung, R.T.K. Baker, J.A. Horsley, Science 211 (1981) 1121.
[30] P.W. Jacobs, F.H. Ribeiro, G.A. Somorjai, S.J. Wind, Catal. Lett. 37 (1996) 131.
[31] P.W. Jacobs, S.J. Wind, F.H. Ribeiro, G.A. Somorjai, Surf. Sci. 372 (1997) L249.
[32] T. Tsirlin, J. Zhu, J. Grunes, G.A. Somorjai, Top. Catal 19 (2002) 165.
[33] A.S. Eppler, J. Zhu, E.A. Anderson, G.A. Somorjai, Top. Catal 13 (2000) 33.
[34] J. Zhu, G.A. Somorjai, Nano Lett. 1 (2001) 8.
[35] J. Grunes, J. Zhu, E.A. Anderson, G.A. Somorjai, J. Phys. Chem. B 106 (2002) 11463.
[36] F. Zaera, G.A. Somorjai, J. Am. Chem. Soc. 106 (1984) 2288.
[37] P. Chen, S. Westerberg, K.Y. Kung, J. Zhu, J. Grunes, G.A. Somorjai, Appl. Catal. A 229 (2002) 147.
[38] J. Grunes, J. Zhu, M.C. Yang, G.A. Somorjai, Catal. Lett. 86 (2003) 157.
[39] Y.K. Choi, J. Zhu, J. Grunes, J. Bokor, G.A. Somorjai, J. Phys. Chem. B 107 (2003) 3340.
[40] J. Grunes, Ph.D. Thesis, University of California, Berkeley, 2004.
[41] J. Grunes, J. Zhu, A. Contreras, Y.K. Choi, J. Bokor, G.A. Somorjai, in: Proceedings of the Second International Conference on Nanoimprint and Nanoprint Technology, Boston, MA, 2003.
[42] R.R. Schlittler, J.W. Seo, J.K. Gimzewski, C. Durkan, M.S.M. Saifullah, Science 292 (2001) 1136.
[43] M. Kolbel, R.W. Tjerkstra, J. Brugger, C.J.M. Van Rijn, W. Nijdam, J. Huskens, D.N. Reinhoudt, Nano Lett. 2 (2000) 1339.
[44] T. Teranishi, M. Hosoe, T. Tanaka, M. Miyake, J. Phys. Chem. B 103 (1999) 3818.
[45] Y. Wang, J. Ren, K. Deng, L. Gui, Y. Tang, Chem. Mater. 12 (2000) 1622.
[46] T.S. Ahmadi, Z.L. Wang, T.C. Green, A. Henglein, M.A. El-Sayed, Science 272 (1996) 1924.
[47] Z. Konya, V.F. Puntes, I. Kiricsi, J. Zhu, P. Alivisatos, G.A. Somorjai, Catal. Lett. 81 (2002) 137.
[48] Z. Konya, V.F. Puntes, I. Kiricsi, J. Zhu, A.P. Alivisatos, G.A. Somorjai, Nano Lett. 2 (2002) 907.
[49] D. Zhao, Q. Huo, J. Feng, Q. Huo, N. Melosh, G.H. Fredrickson, B.F. Chmelka, G.D. Stucky, Science 279 (1999) 548.
[50] R.M. Rioux, H. Song, J.D. Hoefelmeyer, P. Yang, G.A. Somorjai, J. Phys. Chem. B 2005, in press.
[51] R.M. Watwe, B.E. Spiewak, R.D. Cortright, J.A. Dumesic, J. Catal. 180 (1998) 184.
[52] R.M. Watwe, R.D. Cortright, J.K. Nørskov, J.A. Dumesic, J. Phys. Chem. B 104 (2000) 2299.
[53] R.M. Rioux, H. Song, P. Yang, G.A. Somorjai, in preparation.
[54] Y. Yin, R.M. Rioux, C.K. Erdonmez, S. Hughes, G.A. Somorjai, A.P. Alivisatos, Science 304 (2004) 711.
[55] A.D. Simgelskas, E.O. Kirkendall, Trans. AIME 171 (1947) 130.
[56] N.S. Sobal, U. Ebels, H. Möhwald, M. Giersig, J. Phys. Chem. 107 (2003) 7351.
[57] R.D. Cortright, S.A. Goddard, J.E. Rekoske, J.A. Dumesic, J. Catal. 127 (1991) 342.